

# Wannier states and Bose-Hubbard parameters for 2D optical lattices

P. Blair Blakie\*

*Department of Physics, University of Otago, P.O. Box 56, Dunedin, New Zealand and  
Electron and Optical Physics Division, National Institute of Standards and Technology, Gaithersburg, MD 20899-8410.*

Charles W. Clark

*Electron and Optical Physics Division, National Institute of Standards and Technology, Gaithersburg, MD 20899-8410.*

(Dated: 30th October 2018)

We consider the physical implementation of a 2D optical lattice with schemes involving 3 and 4 light fields. We illustrate the wide range of geometries available to the 3 beam lattice, and compare the general potential properties of the two lattice schemes. Numerically calculating the band structure we obtain the Wannier states and evaluate the parameters of the Bose-Hubbard models relevant to these lattices. Using these results we demonstrate lattices that realize Bose-Hubbard models with 2, 4, or 6 nearest neighbors, and quantify the extent that these different lattices effect the superfluid to Mott-insulator transition.

PACS numbers: 03.75.Hh, 32.80.Lg, 03.75.Lm

## I. INTRODUCTION

There has been considerable recent interest in the study of ultra-cold bosonic atoms in optical lattices. The many favorable attributes of optical lattices, such as the absence of defects, low noise level, and high degree of experimental control, are ideal for precise quantum manipulation. As such, this system features in theoretical proposals for quantum computing (e.g. see [1, 2]), simulating many-body systems [3], and studying quantum-phase transitions [4]. Beyond bosons, work by Hofstetter *et al.* [5] suggests using an optical lattice to facilitate the superfluid transition in a degenerate gas of fermionic atoms [5].

Experimental studies with optical lattices have demonstrated many impressive results, including number-squeezing an initially coherent Bose-field using a 1D lattice [6]; the superfluid to Mott-insulator transition in a 3D lattice [7]; the collapse and revival of coherence in a matter-wave field [8]; controlled collisions using state selective lattices [9]. All of these experiments are carried out at sufficiently low temperatures and in deep enough lattices that the constituent bosons occupy only the lowest band, and are well described by a tight-binding Bose-Hubbard model [10]. In this model the Bose-field is decomposed into a set of localized Wannier states, one at each site of the lattice, and the Hamiltonian is characterized by a few parameters: (i) the number of nearest neighbors surrounding each lattice site, (ii) the tunneling strength between nearest neighbors, and (iii) the strength of the interaction between particles at the same site.

The ground state of the Bose-Hubbard Hamiltonian exhibits a quantum phase transition between superfluid and Mott-insulating states, that depends on the relative size of the aforementioned parameters. The transition to an insulating state has been suggested as a method for preparing a fiducial state of precisely one atom per site, suitable for quantum information processing. Another important application of optical lat-

tices is to produce tightly confining potentials suitable for realizing low dimensional gases. For instance, in [11] a 1D lattice was used to investigate Bose-condensation in a quasi-2D gas, and experiments with 2D lattices [12, 13] have produced correlated 1D gases in the elongated potential tubes at each lattice site. For these systems the tunneling parameters and Wannier states characterize the time scale over which each potential is isolated from neighboring sites, and transverse wavefunction for the particles respectively.

To date most theory, and experiments for quantum-degenerate Bose-gases have used cubic lattices, where the optical potential is produced by orthogonal sets of counter propagating light fields. For this case the lattice potential is separable, and the non-interacting band structure is given by the Mathieu spectrum [14]. In this paper we explore the structure and properties of a more general class of two-dimensional optical lattices for regimes relevant to current experiments. We compare and contrast the usual square separable lattice (arising from two sets of independent laser fields) with a more general non-separable lattice produced from three interfering light fields. To characterize the appropriate Bose-Hubbard models for the lattices considered we numerically evaluate the localized Wannier states from band structure calculations. We discuss favorable properties of the 3 beam lattice that make it more ideal for investigating the strongly correlated regime. In particular, we show that certain 3 beam lattice configurations provide tighter on-site confinement, control over the number of nearest neighbors, and significantly reduced tunneling between sites compared to the counter propagating 4 beam arrangement. These properties of the 3 beam lattice lead to the superfluid to Mott-insulator transition occurring for much shallower lattices, and would facilitate taking experiments deeper into the Mott-insulating regime. We also show that by using non-counter propagating light fields in the 4 beam lattice, the depth at which the Mott-transition occurs can be significantly reduced, albeit with the requirement of an additional light field.

Conservative two dimensional optical lattices are an important tool for the emerging field of quantum atom-optics, with numerous practical applications [3, 12, 13, 15]. We see

---

\*Electronic address: bblakie@physics.otago.ac.nz

the calculations presented in this paper as serving two important purposes. First, for people studying the idealized Bose-Hubbard model, these results will elucidate the typical range of Bose-Hubbard parameters accessible, and demonstrate the flexibility of the optical lattice system. Second, we believe these results will be important in design considerations for future experiments with ultra-cold gases in optical lattices.

## II. FORMALISM

### A. Optical Lattice

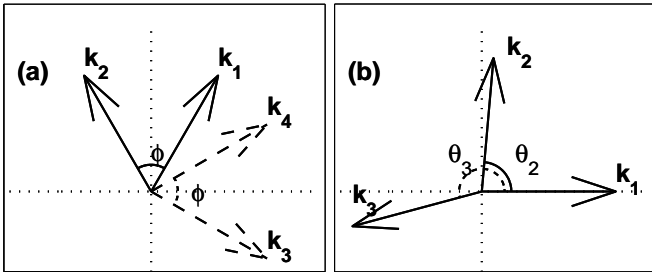


Figure 1: Wave vectors of the laser configurations used to generate a 2D optical lattice. (a) 4 beam lattice formed by two independent sets of plane-wave light fields. Different line types are used to differentiate the two pairs. (b) 3 beam lattice produced by three interfering plane-wave fields. The angles are discussed in the text.

We consider an optical lattice produced from a set of monochromatic plane-waves with propagation directions characterized by their wave vectors  $\{\mathbf{k}_j\}$ . To simplify our discussion of 2D optical lattices we take these propagation directions to all lie in a single plane, which we designate as the  $x$ - $y$  plane. For simplicity we consider all light fields to be linearly polarized along  $z$  and of equal intensity, with the focus of this work on the control of lattice geometry obtained by varying the light field propagation directions. The lattice potential experienced by the atoms is proportional to the real part of the dynamic polarizability  $\alpha$  [22], and the light field intensity  $I_0$  [23]. Below we discuss the two different laser configurations we compare in this paper.

**4 Beam Square Lattice** In Fig. 1(a) we show the geometry used to realize the 2D optical lattice we refer to as the 4 beam (4B) square lattice. This type of lattice (and its 3D generalization) has been extensively employed in recent experiments for the case where each pair of lasers is counter propagating (i.e. with  $\phi = 180^\circ$ ) [7, 15]. The two pairs of light fields are made independent from each other by detuning the common frequency in one pair of fields from that of the other pair. Typically, a negligible frequency difference compared to the optical frequency is required to achieve independence (e.g. see [16]), so to a good approximation all wave-vectors are the same magnitude  $|\mathbf{k}_j| \approx k \equiv 2\pi/\lambda$ , where  $\lambda$  is the optical wavelength. The resulting potential is a superposition of two perpendicular 1D lattices (one arising from each pair),

and in the counter propagating case the lattice site separation is  $\lambda/2$ . As illustrated in Fig. 1(a), we have generalized this arrangement from counter propagating beams to consider the pairs of light fields propagating at symmetrically distributed angles with respect to the coordinate axes. As shown below, this generalization allows control over the distance between lattice sites.

The lattice potential for this arrangement can be written as

$$V_{\text{Latt}}(\mathbf{r}) = \frac{1}{2}V_0 \cos(\mathbf{b}_1 \cdot \mathbf{r}) + \frac{1}{2}V_0 \cos(\mathbf{b}_2 \cdot \mathbf{r}), \quad (1)$$

where

$$\mathbf{b}_1 \equiv \mathbf{k}_1 - \mathbf{k}_2 = 2k \sin(\phi/2)\hat{\mathbf{x}}, \quad (2)$$

$$\mathbf{b}_2 \equiv \mathbf{k}_3 - \mathbf{k}_4 = 2k \sin(\phi/2)\hat{\mathbf{y}}, \quad (3)$$

are the reciprocal lattice vectors and  $V_0 = -\text{Re}\{\alpha\}I_0/2\epsilon_0 c$  is four times the dipole shift associated with a single laser of intensity  $I_0$ . We will refer to  $|V_0|$  as the *light-shift strength*, and note that  $|V_0|$  is the potential depth for the 1D lattice produced by two intersecting light fields of equal intensity  $I_0$ . In more than one spatial dimension the potential saddle point between sites is the most essential characterization of the *lattice depth*, however this depends strongly on the lattice geometry and is difficult to characterize. To be of most relevance to experiments, in this paper we will compare different lattices made with the same light-shift strength  $V_0$ , i.e. produced by sets of laser fields with the same intensity. We note that  $V_0$  can be a positive or negative quantity depending on whether the light fields are blue or red detuned from atomic resonance respectively. The 4 beam lattice is symmetric with respect to  $V_0$  changing sign (to within an overall translation of the lattice), however the next lattice we consider is not.

The direct lattice vectors which specify the translation vectors between lattices sites are

$$\mathbf{a}_1 = \frac{\lambda}{2} \csc(\phi/2)\hat{\mathbf{x}}, \quad (4)$$

$$\mathbf{a}_2 = \frac{\lambda}{2} \csc(\phi/2)\hat{\mathbf{y}}, \quad (5)$$

demonstrating that the lattice site spacing can be varied from  $\lambda/2 \rightarrow \infty$  as  $\phi$  changes from  $180^\circ \rightarrow 0$ .

**3 Beam Lattice** The second 2D optical lattice we consider consists of 3 laser fields — the minimum number needed to generate a 2D lattice. We will refer to this configuration as the 3 beam (3B) lattice. The geometric arrangement of the light fields is shown in Fig. 1(b), with all three light fields taken to have the same frequency. The lattice potential, for this arrangement, given by

$$V_{\text{Latt}}(\mathbf{r}) = \frac{1}{2}V_0 \cos(\mathbf{b}_1 \cdot \mathbf{r}) + \frac{1}{2}V_0 \cos(\mathbf{b}_2 \cdot \mathbf{r}) + \frac{1}{2}V_0 \cos([\mathbf{b}_1 + \mathbf{b}_2] \cdot \mathbf{r}), \quad (6)$$

is a sum of three 1D lattices arising from the interference between each distinct pair of fields. As for the 4 beam case, we have introduced the light-shift strength parameter  $V_0 =$

$-\text{Re}\{\alpha\}I_0/2\epsilon_0c$ , and we define the reciprocal lattice vectors  $\mathbf{b}_j$  below.

The incident wave-vectors are of the form

$$\mathbf{k}_j = k[\cos\theta_j\hat{\mathbf{x}} + \sin\theta_j\hat{\mathbf{y}}], \quad (7)$$

and generate a potential that exhibits a broad range of crystallographic configurations, dependent on the choice of  $\{\theta_1, \theta_2, \theta_3\}$ . The crystallography of this type of lattice has been considered by Petsas *et al.* [17] in a context relevant to laser cooling atoms, however we find it useful to cast their observations in an analytic framework relevant to conservative lattices. To do this we choose to label our wave vectors such that  $\theta_1 < \theta_2 < \theta_3$ , and place the following restrictions on the angles:

$$\theta_1 = 0, \quad (8)$$

$$0 < \theta_2 < 180^\circ, \quad (9)$$

$$0 < \theta_3 - \theta_2 < 180^\circ, \quad (10)$$

For any set of three coplanar light fields (excluding the case where two beams are co-propagating which gives rise to a 1D lattice) the angles can always be transformed to satisfy requirements (8)-(10) with an overall rotation the system in the  $x$ - $y$  plane.

Analogously to what was done in the four beam lattice, we define the reciprocal lattice vectors as

$$\mathbf{b}_j = \mathbf{k}_j - \mathbf{k}_{j+1} \quad (j = 1, 2). \quad (11)$$

We note that other choices of reciprocal lattice vectors are possible. The direct lattice vectors  $\{\mathbf{a}_1, \mathbf{a}_2\}$  can then be determined from the orthogonality relationship  $\mathbf{a}_i \cdot \mathbf{b}_j = 2\pi\delta_{ij}$  (e.g. see [18]). For the purposes of discussing direct lattice geometry, it is useful to specify the angle  $\phi_D$  between the direct lattice vectors and the ratio of their lengths  $r_D$ . It can be shown that these relate to the incident laser angles as

$$\phi_D = 180^\circ - \frac{\theta_3}{2}, \quad (12)$$

$$r_D \equiv \frac{|\mathbf{a}_2|}{|\mathbf{a}_1|} = \frac{\sin(\theta_2/2)}{\sin((\theta_3 - \theta_2)/2)}. \quad (13)$$

This expression can be inverted to uniquely determine the laser angles under restrictions (8)-(10) for  $r_D \in (0, \infty)$ , and  $\phi_D \in (\cos^{-1}(1/r_D), 180^\circ)$ .

Finally, we note that unlike the 4 beam potential, the 3 beam potential (6) is not symmetric with respect to sign change of  $V_0$  (i.e. change in the sign of the laser detuning from atomic resonance), a point we elaborate on in Sec. III. The 3 beam lattice only realizes a periodic set of confining wells for the case of red detuning, i.e.  $V_0 < 0$ , and as such we restrict our attention to red-detuned lattices in this paper.

## B. Wannier states

The eigenstates of the periodic single particle Hamiltonian,

$$\hat{H}_0 = \hat{\mathbf{p}}^2/2m + V_{\text{Latt}}(\mathbf{r}), \quad (14)$$

are known as Bloch states, which we write as  $\psi_{n\mathbf{q}}(\mathbf{r})$ , with respective energy eigenvalue  $\hbar\omega_{n\mathbf{q}}$ . Here we take the lattice potential to be a general periodic function on the Bravais lattice of points  $\mathbf{R}_j = n_{1j}\mathbf{a}_1 + n_{2j}\mathbf{a}_2$  ( $n_{ij} \in \mathbb{Z}$ ), such that  $V_{\text{Latt}}(\mathbf{r}) = V_{\text{Latt}}(\mathbf{r} + \mathbf{R}_j)$ . According to Bloch's theorem, these eigenstates can be written as

$$\psi_{n\mathbf{q}}(\mathbf{r}) = u_{n\mathbf{q}}(\mathbf{r})e^{i\mathbf{q}\cdot\mathbf{r}}, \quad (15)$$

where  $u_{n\mathbf{q}}(\mathbf{r}) = u_{n\mathbf{q}}(\mathbf{r} + \mathbf{a}_i)$  is a periodic function,  $\mathbf{q}$  is the quasi-momentum, and  $n$  is the band index. Formally, a Bravais lattice is of infinite extent, however it is numerically convenient for us to consider a finite lattice of  $N$  sites with periodic boundary conditions. For this situation each energy band contains  $N$  eigenstates, and the quasi-momenta can be restricted to the first Brillouin zone.

Bloch states are extended states that span the entire lattice. To consider many-body effects arising from the interactions between particles it is more convenient to work with a set of localized states. Here we consider the Wannier basis which is a unitary transformation of the Bloch basis, where the basis states are labeled by lattice site position. The Wannier state centered at site  $\mathbf{R}_i$  is defined as

$$w_n(\mathbf{r} - \mathbf{R}_i) \equiv \frac{1}{\sqrt{N}} \sum_{\mathbf{q}} e^{-i\mathbf{q}\cdot\mathbf{R}_i} \psi_{n\mathbf{q}}(\mathbf{r}), \quad (16)$$

where the summation is taken over all Bloch states of band- $n$ . For describing quantum degenerate Bose-gases in optical lattices we will only consider Wannier states of the ground band.

Wannier states are not eigenstates of the Hamiltonian and so an atom prepared into a Wannier state at a given site will tunnel to other Wannier states over time. This tunneling between sites is characterized by the matrix elements of the Hamiltonian between the respective Wannier states at those sites, i.e.

$$\gamma_{\mathbf{R}_i - \mathbf{R}_j} \equiv \int d\mathbf{r} w_0^*(\mathbf{r} - \mathbf{R}_i) \hat{H}_0 w_0(\mathbf{r} - \mathbf{R}_j), \quad (17)$$

which reduces to

$$\gamma_{\mathbf{R}_i - \mathbf{R}_j} \equiv \frac{1}{N} \sum_{\mathbf{q}} \hbar\omega_{n\mathbf{q}} e^{-i\mathbf{q}\cdot(\mathbf{R}_j - \mathbf{R}_i)}, \quad (18)$$

i.e. the Fourier transform of the Bloch dispersion relation. We note that the overlap integral between states at different sites (18) only depends on the relative separation between the sites, so that characterizing the tunneling properties of a single Wannier state completely determines the matrix elements of the whole lattice.

For deep lattices the Wannier state is well localized at its central site and  $\gamma_{\mathbf{R}}$  rapidly decreases with increasing relative separation  $|\mathbf{R}|$ . This is the well-known tight binding limit, where a state at any given site only couples (to any degree of significance) to a few neighboring sites. In this limit only the most prominent tunneling matrix elements to other sites are retained, where these sites are referred to as the *nearest neighbors*. For cases where the nearest neighbor tunneling terms are all equal it is conventional to define the tunneling

parameter or hopping rate as  $J = -\gamma_{\mathbf{R}_j}$  (e.g. see [4]). We will present quantitative results for these tunneling rates and demonstrate systems which exhibit different numbers of nearest neighbors in Sec. IV.

### C. Bose-Hubbard model

Here we review the Bose-Hubbard model for interacting Bosonic atoms in an optical lattice, closely following the original derivation by Jaksch *et al.* [4]. The usual starting point for discussing many-body aspects of ultra-cold atoms is the second quantized Hamiltonian

$$\hat{H} = \int d\mathbf{r} \hat{\psi}^\dagger(\mathbf{r}) \left\{ \hat{H}_0 + V_{\text{ext}}(\mathbf{r}) \right\} \hat{\psi}(\mathbf{r}) + \frac{1}{2}g \int d\mathbf{r} \hat{\psi}^\dagger(\mathbf{r}) \hat{\psi}^\dagger(\mathbf{r}) \hat{\psi}(\mathbf{r}) \hat{\psi}(\mathbf{r}), \quad (19)$$

where  $\hat{\psi}(\mathbf{r})$  is the boson field operator,  $V_{\text{ext}}(\mathbf{r})$  describes a slowly varying external potential (in addition to the lattice potential in  $\hat{H}_0$ ),  $g = 4\pi\hbar^2 a_s/m$  is the interaction strength, with  $a_s$  the scattering length and  $m$  the atomic mass.

If a sample of sufficiently cold Bosonic atoms is loaded into a deep enough lattice (e.g. from a Bose-Einstein condensate), then only states of the lowest vibrational band will be populated. This system is conveniently described by expanding the field operators in the Wannier basis of the ground band

$$\hat{\psi}(\mathbf{r}) = \sum_i w_0(\mathbf{r} - \mathbf{R}_i) \hat{a}_i, \quad (20)$$

where the operator  $\hat{a}_i$  destroys a particle in the  $\mathbf{R}_i$ -Wannier orbital, and satisfies the usual Bose commutation relations  $[\hat{a}_i, \hat{a}_j] = 0$  and  $[\hat{a}_i, \hat{a}_j^\dagger] = \delta_{ij}$ . In the Wannier representation the Hamiltonian (19) reduces to the Bose-Hubbard form

$$\hat{H} \approx -J \sum_{\langle i,j \rangle} \hat{a}_i^\dagger \hat{a}_j + \sum_i \epsilon_i \hat{a}_i^\dagger \hat{a}_i + \frac{1}{2} U_{\text{BH}} \sum_i \hat{a}_i^\dagger \hat{a}_i^\dagger \hat{a}_i \hat{a}_i, \quad (21)$$

where the first summation in Eq. (19) has been restricted to the nearest neighbor sites (i.e. tight binding approximation discussed above). We have also introduced the site dependent local energy

$$\epsilon_i \equiv \int d\mathbf{r} w_0^*(\mathbf{r} - \mathbf{R}_i) V_{\text{ext}}(\mathbf{r}) w_0(\mathbf{r} - \mathbf{R}_i), \quad (22)$$

$$\simeq V_{\text{ext}}(\mathbf{R}_i) \quad (23)$$

and the on-site interaction term

$$U_{\text{BH}} \equiv g \int d\mathbf{r} |w_0(\mathbf{r})|^4. \quad (24)$$

The Bose-Hubbard model will be a good description of the system if degrees of freedom in the higher bands can

be neglected. For an energy gap to the first excited band of  $E_{\text{gap}}$ , we find the validity conditions to be  $k_B T \ll E_{\text{gap}}$  and  $n U_{\text{BH}} \ll E_{\text{gap}}$ , where  $n$  is the average site occupation. Typically these requirements are well satisfied in experiments.

In this paper we calculate 2D Bose-Hubbard model parameters that can be achieved using a 2D optical lattice. The nature of the confinement transverse to the lattice will have considerable influence on the physical properties of the system, however this is beyond the scope of this paper. For simplicity we assume that the motion transverse to the lattice is frozen out, e.g. as could be arranged experimentally by superimposing a deep 1D lattice to slice the potential tubes of the 2D lattice into a set of independent planes.

### D. Superfluid to Mott-insulator transition

One of the most fascinating properties of the Bose-Hubbard Hamiltonian is that it predicts a quantum-phase transition of the ground state of the system between superfluid and Mott-insulating states [10]. The phase diagram for the system depends precisely on the Bose-Hubbard parameters and the average filling factor of the system. It is convenient to define the dimensionless quantity

$$\eta \equiv \frac{U_{\text{BH}}}{zJ}, \quad (25)$$

embodying the Bose-Hubbard model parameters, where  $z$  is the number of nearest neighbors. For a homogeneous system with unit filling (i.e. an average density of one boson per site), a critical value of  $\eta_c \approx 5.8$  is predicted by mean-field theories for the transition [24]. For  $\eta < \eta_c$  the system is in a superfluid state where the hopping between sites dominates over on-site repulsion. In this state, the system exhibits phase coherence across the lattice and significant fluctuations in the number of bosons per site. For  $\eta > \eta_c$  interaction effects dominate tunneling and the particles become localized — this is the Mott-insulator state, characterized by a near definite number of particles per site and an absence of phase coherence between sites.

For bosonic atoms in an optical lattice the values of  $U_{\text{BH}}$  and  $J$  can be dynamically modified by changing the lattice depth. E.g. the effect of increasing the lattice depth is to confine the bosons more tightly at each site, increasing  $U_{\text{BH}}$ , and reducing the tunneling between sites. Greiner *et al.* [7] have experimentally demonstrated a loading procedure that is sufficiently adiabatic for the system to be reversibly taken through the phase transition.

## III. LATTICE GEOMETRY

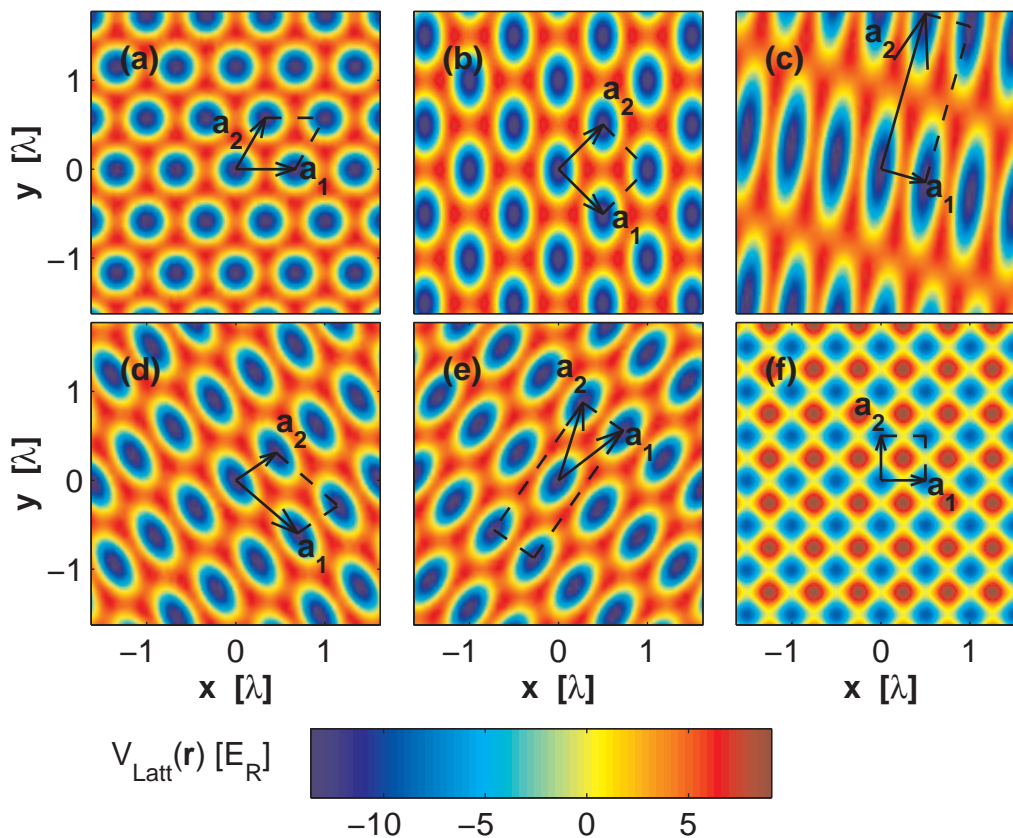


Figure 2: Optical lattice potentials. (a)-(e) Potentials for the 3 beam laser configuration. (f) Potential for the 4 beam counter propagating configuration. For these plots  $V_0 = -9E_R$ , other parameters discussed in the text.

In Fig. 2 we demonstrate a variety of the possible 2D optical lattice geometries that can be made with the lattice types discussed in Sec. II A. In particular, the 3 beam configuration allows the five distinct types of two-dimensional Bravais lattices to be realized by suitably choosing the incident light field angles (Figs. 2(a)-(e)). In Fig. 2(f) we show the counter propagating 4 beam lattice potential. Note that we have chosen to specify light-shift strength in units of photon recoil energy, defined as  $E_R = \hbar^2 k^2 / 2m$ .

In more detail the cases considered in Fig. 2 are (named according to the underlying Bravais lattice geometry):

- (a) **[3 Beam] Hexagonal Lattice:** This highly symmetric triangular lattice displays hexad symmetry (symmetry under  $60^\circ$  rotations). This lattice naturally arises in close packing of spheres - and corresponds to the planes of three dimensional hexagonal close-packed and face-centered cubic lattices [18]. The direct lattice vectors have length ratio  $r_D = 1$  and intersect at an angle of  $\phi_D = 60^\circ$ . The light fields needed to make this lattice have planar angles of  $\theta_2 = 120.0^\circ$  and  $\theta_3 = 240.0^\circ$  (see Eqs. (12) and (13)).
- (b) **[3 Beam] Square Lattice:** This square lattice has an underlying Bravais lattice with tetrad symmetry (symmetric under  $90^\circ$  rotations), though the potential does

not exhibit this symmetry (it is only symmetric under  $180^\circ$  rotations). The direct lattice vectors have length ratio  $r_D = 1$  and intersect at an angle of  $\phi_D = 90^\circ$ . The light fields needed to make this lattice have planar angles of  $\theta_2 = 90.0^\circ$  and  $\theta_3 = 180.0^\circ$ .

- (c) **[3 Beam] Rectangular Lattice:** The rectangular lattice emphasizes the considerable asymmetry between directions that can be engineered. For the specific case we have chosen to consider the direct lattice vectors have length ratio  $r_D = 3.5$  and intersect at an angle of  $\phi_D = 90^\circ$ . The large lattice vector  $\mathbf{a}_2$  arises because the light fields with wavevector  $\mathbf{k}_2$  and  $\mathbf{k}_3$  differ by a relatively small angle of  $31.9^\circ$ , i.e.  $\theta_2 = 148.1^\circ$  and  $\theta_3 = 180.0^\circ$ .
- (d) **[3 Beam] Oblique Lattice:** This is the most general planar lattice type of which all other 2D Bravais lattices are special cases. The only symmetry that this lattice exhibits in general is diad symmetry (symmetric under  $180^\circ$  rotations). For the specific case considered, the direct lattice vectors have length ratio  $r_D = 0.6$  and intersect at an angle of  $\phi_D = 85^\circ$ . The light fields needed to make this lattice have planar angles of  $\theta_2 = 64.5^\circ$  and  $\theta_3 = 190.0^\circ$ .

- (e) **[3 Beam] Centered Rectangular Lattice:** The centered rectangular lattice is usually specified using the larger (non-primitive) cell indicated in Fig. 2(e), that emphasizes the presence of a face centered point. For the specific case considered, the direct lattice vectors have length ratio  $r_D = 1$  and intersect at an angle of  $\phi_D = 35^\circ$ . The light fields needed to make this lattice have planar angles of  $\theta_2 = 145.0^\circ$  and  $\theta_3 = 290.0^\circ$ .
- (f) **[4 Beam] Square Lattice:** This lattice is formed from two sets of counter propagating light fields with a  $\lambda/2$  lattice site spacing, and exhibits the highest lattice site density (per unit area) of the lattices considered in Fig. 2.

Before considering the Wannier states of these lattices it is useful to compare the most significant differences between the 3 beam and 4 beam lattices.

*Lattice geometry:* As demonstrated in Figs. 2(a)-(e), the 3 beam lattice exhibits a wide range of lattice types, with the laser angles calculated using expressions (12) and (13). The rigid constraints we placed upon the light field arrangement of the 4 beam lattice ensures the resulting lattice is square. Relaxing these constraints by allowing the relative intersection angle of each pair to be different, or apply an overall rotation to one pair, it is possible to generate rectangular or oblique lattices respectively. These generalizations are not considered in this work.

The lattice geometry plays a central role in determining the number of nearest neighbors,  $z$ , in the derived Bose-Hubbard model. Inspection of Fig. 2 suggests that the 3 beam lattice offers cases that realize 2 (see Fig. 2(c)), 4 (see Fig. 2(b)), and 6 (see Fig. 2(a)) nearest neighbors. With the aid of band structure calculations for the tunneling matrix elements we return to this issue in the next section, and verify the actual numbers of nearest neighbors. Another important factor relating to the geometry is the distance between lattice sites. For the 4 beam lattice (Fig. 2(f)) the spacing between sites is the minimum value of  $|\mathbf{a}_j| = \lambda/2$ . For the 3 beam lattice spacing is generally larger, e.g.  $|\mathbf{a}_j| = 2\lambda/3$  for the hexagonal lattice (Fig. 2(a)),  $|\mathbf{a}_j| = \lambda/\sqrt{2}$  in the square lattice (Fig. 2(b)). The site spacing will influence the tunneling between sites, as this is strongly dependent on the *barrier width* between sites.

*Unit cell potential shape:* The single well potential for the 3 beam and 4 beam lattices are quite distinctive, as is illustrated for two particular cases in Fig. 3. The most noticeable feature distinguishing these cases (and is a general observation for the different configurations of 3 beam lattice) is that

the saddle point of the potential separating a given lattice site from the neighboring site is much higher in the 3 beam lattice (Fig. 3(a)) than in the 4 beam lattice (Fig. 3(b)). The superior confinement of the 3 beam lattice produces much better localized Wannier states than for a 4 beam lattice with the same lattice site spacing and field intensity (per incident beam), as we demonstrate in the next section. From Fig. 3(a) it is clear why the 3 beam lattice is not symmetric with respect to  $V_0$  changing sign: The subtle crown-like maxima of the 3 beam lattice (which become the minima when the light fields are changed to blue detuning) are shallow and provide little confinement. The dominant feature for the blue detuned 3 beam lattice is the periodic array of maxima, referred to as an *anti-dot* lattice (e.g. see [19]).

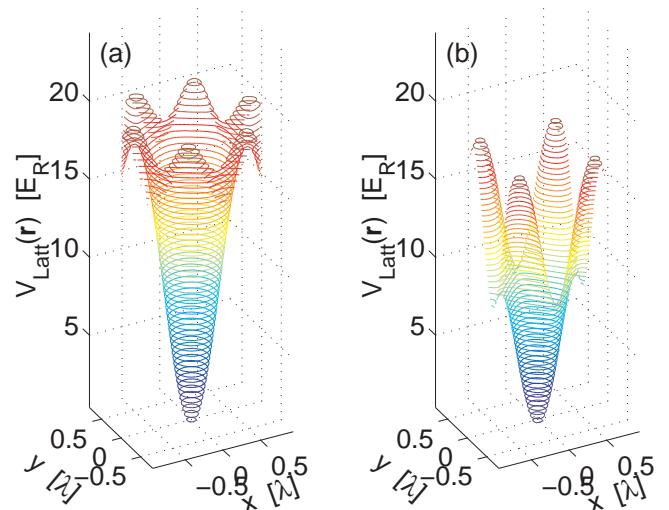


Figure 3: Comparison of the individual potential wells of the 3 beam and 4 beam lattices. Potential energy contour plot of (a) 3 beam hexagonal lattice, and (b) 4 beam square lattice. The potentials are displayed on a region of space slightly larger than a primitive unit cell. The lattice potentials displayed here correspond to the same configurations and parameters used in Figs. 2(a) and (f) respectively. An energy offset has been added so that the potential minima are at 0.

#### IV. WANNIER STATES AND BOSE-HUBBARD PARAMETERS

In this section we present numerical calculations of the Wannier states and Bose-Hubbard parameters for the different 2D optical lattices considered in this paper.

To begin, we briefly summarize our numerical procedures. We diagonalize the non-interacting lattice Hamiltonian (14) represented in a plane-wave expansion to obtain the ground

band Bloch states and energy eigenvalues for each quasi-momentum value within the first Brillouin zone. Ensuring the Bloch states are continuous in quasi-momentum, we construct the Wannier states by numerically summing the Bloch states with the appropriate phase factors (see Eq. (16)). Having obtained the Wannier states, the on-site interaction can be

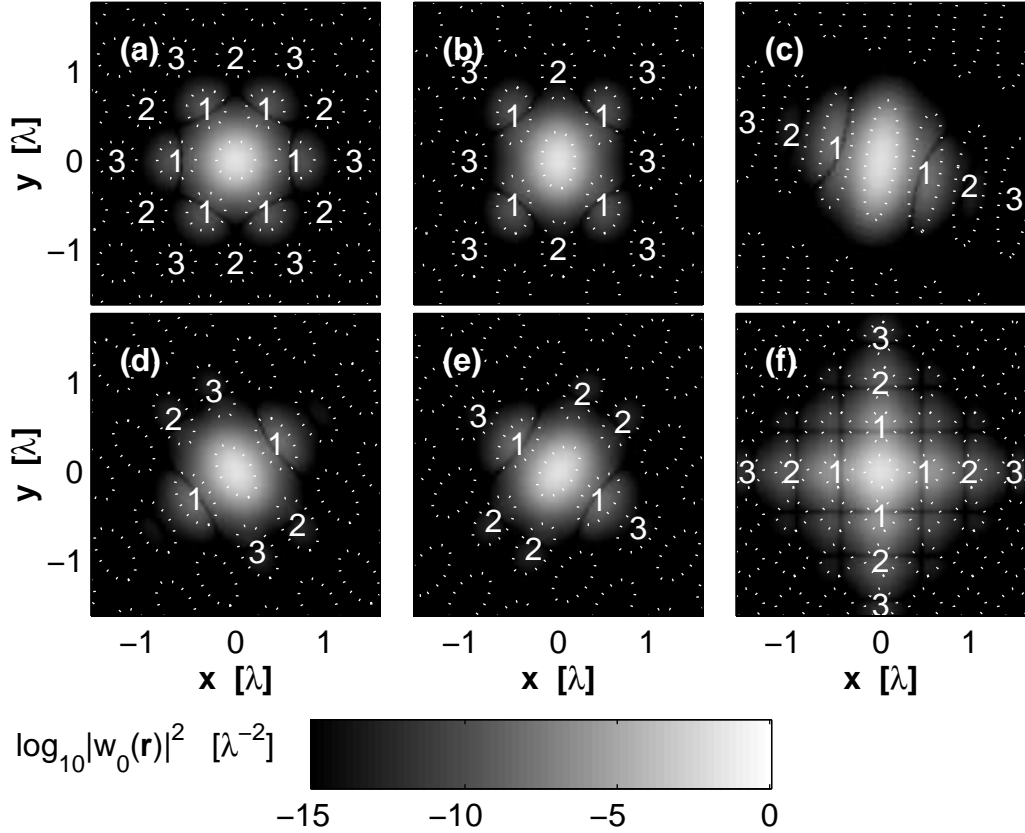


Figure 4: Wannier state density distributions and tunneling neighborhoods. The log-densities of the Wannier states in (a)-(f) correspond to the similarly labeled potentials displayed in Fig. 2. Potential energy contours are indicated by dotted white lines mark the lattice site locations. The white numbers centered upon neighboring sites denote the ‘nearness’ of that site according to a ranking of the tunneling matrix elements (see text). For these plots  $V_0 = -9E_R$ .

evaluated according to Eq. (24) using numerical integration. Finally, the tunneling matrix elements are calculated from the ground band energy spectrum using Eq. (18). We note that to numerically calculate the tunneling matrix elements couplings,  $\gamma_{\mathbf{R}_i - \mathbf{R}_j}$ , we need to take the lattice size  $N$  to be sufficiently large to contain the sites  $\mathbf{R}_i$  and  $\mathbf{R}_j$ .

The Wannier state localized at the origin site for each of the six lattice potentials of Fig. 2 are shown in Fig. 4. At the light-shift strength considered ( $V_0 = -9E_R$ ), the Wannier states are all well localized upon the central site, and to facilitate observing the small density tails at the neighboring sites we have employed a log-scale for the density color-map. The Wannier state of the 4 beam square lattice is the least localized of the all the states considered, mainly due to poor degree of lattice site confinement discussed earlier (see Fig. 3(b)). It is interesting to note that the first node in the Wannier states occurs near the middle of the neighboring site, as is required for states at different sites to be orthogonal.

The tunneling matrix elements provide a quantitative measure of the coupling strength between different Wannier states. In order to demonstrate the variable number of nearest neighbors, and the extent to which further than nearest neighbor couplings are negligible, we have listed the tunneling matrix elements in table I and have indicated the groups of sites these

matrix elements correspond to in Fig. 4. To be clear, in Fig. 4 we have enumerated all sites that have the same tunneling matrix element to the central site with the same number, e.g. 1 indicates ‘first nearest neighbor’, 2 indicates ‘2nd nearest neighbor’, etc. (i.e. larger integers indicate decreasing magnitude of tunneling matrix element). These results indicate that at  $V_0 = -9E_R$  the second nearest neighbors have tunneling rates that are 2-4 orders of magnitude smaller than those of the nearest neighbors. Tight-binding can be expected to provide an excellent description of the system in this regime, i.e. we are justified in identifying the first column of Table I with  $-J$  (see Sec. II B), and ignoring all other couplings. Another important observation is that the number of nearest neighbors for the Wannier states in Figs. 4(a)-(f) (i.e. the number of 1’s in each figure) takes the values 2, 4, or 6.

We note that the tunneling to the rows of sites vertically separated from the site at the origin in Fig. 4(c) is so small that it is completely negligible compared to the first three neighbors considered. Also, the separable nature of the potential for the square 4 beam lattice in Fig. (f) means that tunneling to all sites not lying on axis are identically zero.

As a final comparison between the lattices we consider the global variation of the nearest neighbor tunneling and the on-site interaction for a broad range of light-shift strengths. We



site label:	1-sites	2-sites	3-sites
(a) (3B) Hexagonal	$-2.79 \times 10^{-4}$	$8.75 \times 10^{-8}$	$5.64 \times 10^{-8}$
(b) (3B) Square	$-1.862 \times 10^{-4}$	$-1.12 \times 10^{-6}$	$-8.88 \times 10^{-8}$
(c) (3B) Rectangular	$-2.90 \times 10^{-3}$	$4.54 \times 10^{-6}$	$-1.12 \times 10^{-8}$
(d) (3B) Oblique	$-1.83 \times 10^{-3}$	$-6.48 \times 10^{-6}$	$-4.28 \times 10^{-6}$
(e) (3B) Centered	$-1.80 \times 10^{-3}$	$-6.33 \times 10^{-6}$	$1.84 \times 10^{-6}$
(f) (4B) Square	$-2.42 \times 10^{-2}$	$3.77 \times 10^{-4}$	$-9.28 \times 10^{-6}$

Table I: Values of the first three nearest neighbor couplings for the Wannier states considered in Fig. 4 in units of  $E_R$ . The values in the columns labeled “ $j$ -sites” correspond to the tunneling matrix element between the Wannier state at the origin and the sites enumerated by  $j$  in Fig. 4.

have chosen five lattices to make this comparison. The first four lattices are the most unique of those considered in Figs. 2 and 4: (a) the 3 beam hexagonal lattice (6 nearest neighbors); (b) the 3 beam square lattice (4 nearest neighbors); (c) the 3 beam rectangular lattice (2 nearest neighbors); and (f) the 4 beam square lattice (4 nearest neighbors). For the fifth lattice we introduce a new 4 beam configuration with a larger lattice constant of  $|\mathbf{a}_j| = 2\lambda/3$  (for which the pairs of light fields intersect at  $\phi \approx 97.2^\circ$ ), chosen to have the same distance between sites as the hexagonal lattice. Our motivation for considering this lattice is to better assess the extent to which wider spacing between sites in the 4 beam lattice reduces nearest neighbor tunneling.

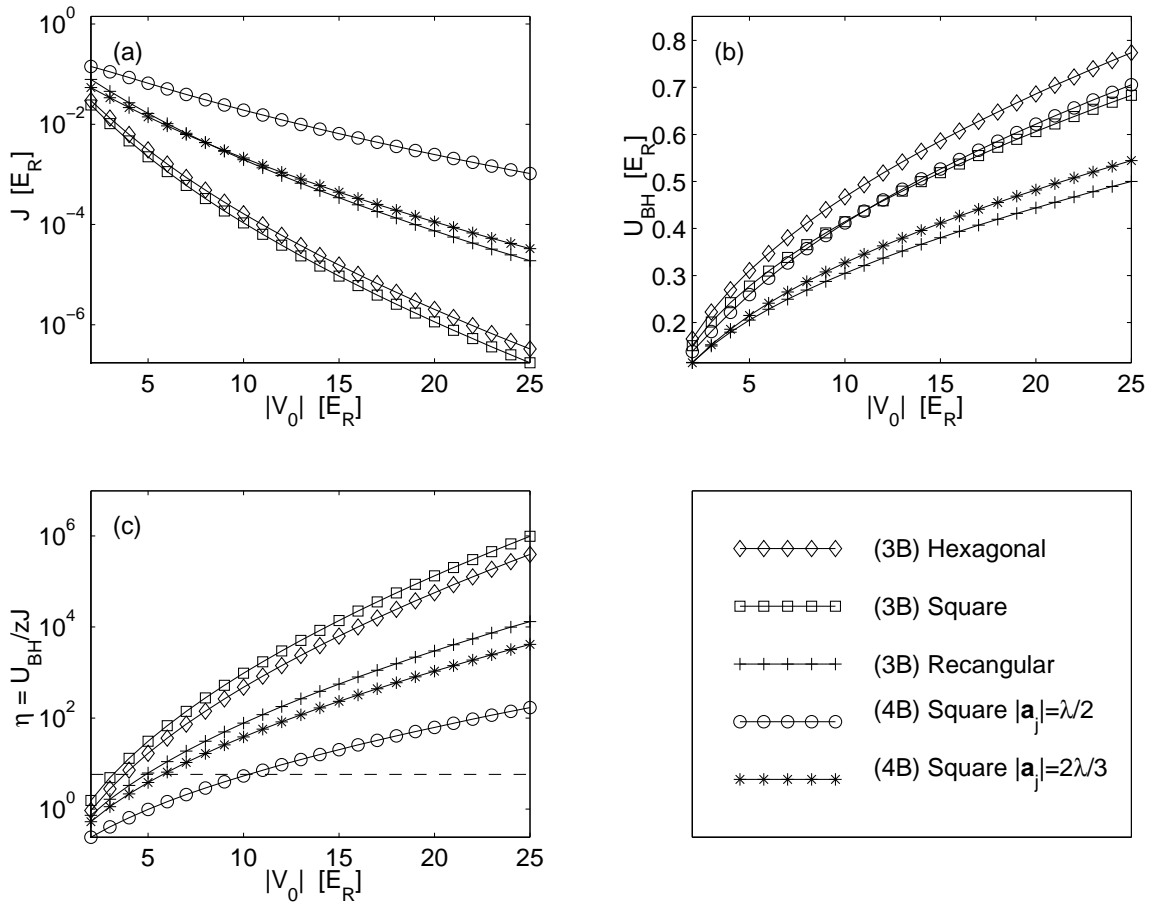


Figure 5: Bose-Hubbard parameters for a variety of different 2D lattices at various light-shift strengths (a) Nearest neighbor tunneling strength. (b) On-site interaction strength. (c) Dimensionless scaling parameter  $\eta$  (see Sec. IID). Dashed horizontal line indicates the critical value for superfluid to Mott-insulator transition for a homogeneous system with filling factor  $n = 1$ . We have taken an effective 2D coupling constant of  $g_{2D} = 0.98 E_R/k^2$  ( $k = 2\pi/\lambda$ ). Note that the coupling strength  $g$ , discussed in Sec. II C, involves the 3D scattering length, so that  $g_{2D}$ , is obtained by integrating over the degree of freedom transverse to the lattice. The value of  $g_{2D}$  we use here assumes the potential transverse to the lattice is a tightly confining harmonic trap of frequency  $\omega_z = \hbar k^2/m$ . We choose physical parameters corresponding to the scattering length of  $^{87}\text{Rb}$  and  $\lambda = 852\text{nm}$  (similar to those of Ref. [7]).

The results for the five chosen lattice types are shown in Fig. 5. In Fig. 5(a) the nearest neighbor tunneling matrix ele-

ments are displayed. Generally the 3 beam lattices have com-



parable or considerably smaller tunneling matrix elements than the 4 beam lattices at any given light-shift strength. In particular, tunneling in the 3 beam square and hexagonal lattices is more than 3 orders of magnitude smaller than the counter propagating 4 beam lattice at the maximum light-shift. Of the 4 beam lattices, the non-counter propagating configuration has significantly smaller tunneling matrix element than the counter propagating configuration at each light-shift strength. Nevertheless, the non-counter propagating 4 beam lattice (with lattice site spacing matching that of the hexagon lattice) has much larger tunneling matrix elements than the hexagonal lattice due to the residual differences in the potentials of the individual wells (see Sec. III).

In Fig. 5(b) we show the on-site interaction strength,  $U_{\text{BH}}$ . It is surprising to note that for the hexagonal lattice  $U_{\text{BH}}$  is higher than that of the counter propagating 4 beam lattice at every value of  $V_0$ , indicating that the hexagonal lattice has tighter lattice site confinement. A useful measure of the confinement is furnished by the oscillation frequency of the harmonic approximation to the lattice site minima. For fixed  $V_0$ , we find that the oscillation frequency of the hexagonal lattice is  $\sim 6\%$  higher than for the counter-propagating 4 beam lattice.

In Fig. 5(c) we plot  $\eta$  (see Eq. (25)), which embodies the parameters of the Bose-Hubbard Hamiltonian. As discussed in Sec. IID, the value of  $\eta$  determines whether the equilibrium ground state is a superfluid or a Mott-insulator. For reference we have indicated the transition point for filling factor  $n = 1$  as a horizontal dashed line in Fig. 5(c). For the lattices considered, the Mott-transition (where the curves cross the dashed line) varies over a wide range of light-shift strengths. In the hexagonal lattice the Mott-transition is at the lowest light-shift of  $|V_0| \approx 3.7E_R$ , whereas the transition for the 4 beam counter propagating lattice occurs at the largest value of  $|V_0| \approx 10.2E_R$ . For reference, this 4 beam lattice is the two dimensional version of the lattice recently used by Greiner *et al.* [7] to experimentally observe the Mott-transition.

Comparing two 4 beam lattices in Figs. 5(a)-(c) yields the following observations. Relative to the  $|\mathbf{a}_j| = \lambda/2$  lattice,

the  $|\mathbf{a}_j| = 2\lambda/3$  lattice has significantly smaller  $J$ , smaller  $U_{\text{BH}}$ , which combined result in a substantially larger  $\eta$  value at each light-shift strength. In general choosing smaller angles between the pairs of light fields  $\phi$  in the 4 beam lattice (see Fig. 1) could be used to maximize  $\eta$ , and reduce the light-shift strength at which the Mott-transition occurs. E.g., for  $\phi = 60^\circ$  the lattice site spacing is  $\lambda$ , and Mott-transition occurs at  $|V_0| \approx 2.5E_R$  — lower than any of the 3 beam curves. However, reducing the transition light-shift strength is made at the expense of  $U_{\text{BH}}$ , the tightness of well site confinement, and the energy gap to higher bands (hence the validity of the Bose-Hubbard description). Balancing these trade offs will be an important consideration for many practical applications.

## V. CONCLUSIONS

In this paper we have investigated different types of 2D optical lattices that might be used in experiments to produce highly correlated states, such as the Mott-insulator state, or to engineer 1D potentials. Through numerical investigation of the band structure and explicit calculation of the Wannier states, we have evaluated the Bose-Hubbard parameters over a wide regime. We have demonstrated lattices that realize Bose-Hubbard models with 2, 4, or 6 nearest neighbors and significantly effect the light-shift strength at which superfluid to Mott-insulator transition occurs.

## Acknowledgments

P.B.B would like to thank J. V. Porto and members of the NIST Laser Cooling Group for useful discussions. This work was supported by the US Office of Naval Research, and the Advanced Research and Development Activity.

- 
- [1] I. Deutsch and P. Jessen, *Phys. Rev. A* **57**, 1972 (1998).
  - [2] T. Calarco, H. Briegel, D. Jaksch, J. I. Cirac, and P. Zoller, *J. of Mod. Opt.* **47**, 2137 (2000).
  - [3] D. Jaksch and P. Zoller, *New J. Phys.* **5**, 56 (2003).
  - [4] D. Jaksch, C. Bruder, J. I. Cirac, C. Gardiner, and P. Zoller, *Phys. Rev. Lett.* **81**, 3108 (1998).
  - [5] W. Hofstetter, J. Cirac, P. Zoller, E. Demler, and M. Lukin, *Phys. Rev. Lett.* **89**, 220407 (2002).
  - [6] C. Orzel, A. K. Tuchman, M. L. Fenselau, M. Yasuda, and M. A. Kasevich, *Science* **23**, 2386 (2001).
  - [7] M. Greiner, O. Mandel, T. Esslinger, T. W. Hänsch, and I. Bloch, *Nature* **415**, 39 (2002).
  - [8] M. Greiner, O. Mandel, T. W. Hänsch, and I. Bloch, *Nature* **419**, 51 (2002).
  - [9] O. Mandel, M. Greiner, A. Widera, T. Rom, T. Hänsch, and I. Bloch, *Phys. Rev. Lett.* **91**, 010407 (2003).
  - [10] M. P. A. Fisher, P. B. Weichman, G. Grinstein, and D. S. Fisher, *Phys. Rev. B* **40**, 546 (1989).
  - [11] S. Burger, F. S. Cataliotti, C. Fort, P. Maddaloni, F. Minardi, and M. Inguscio, *Europhys. Lett.* **57**, 1 (2002).
  - [12] B. Laburthe-Tolra, J. V. Porto, K. M. O'Hara, J. H. Huckans, S. L. Rolston, and W. D. Phillips cond-matt, 0312003 (2003).
  - [13] H. Moritz, T. Stöferle, M. Köhl, and T. Esslinger, *Phys. Rev. Lett.* **91**, 250402 (2003).
  - [14] M. Abramowitz and I. A. Stegun, *Handbook of mathematical functions* (US Government Printing Office, 1964).
  - [15] M. Greiner, I. Bloch, O. Mandel, T. W. Hänsch, and T. Esslinger, *Phys. Rev. Lett.* **87**, 160405 (2001).
  - [16] S. Peil, J. V. Porto, B. L. Tolra, J. M. Obrecht, B. E. King, M. Subbotin, S. L. Rolston, and W. D. Phillips, *Phys. Rev. A* **67**, 051603(R) (2003).
  - [17] K. Petsas, A. Coates, and G. Grynberg, *Phys. Rev. A* **50**, 5173 (1994).
  - [18] N. W. Ashcroft and N. D. Mermin, *Solid State Physics* (W.B.

Saunders Company, 1976).

- [19] K. Petsas, C. Triché, L. Guidoni, C. Jurczak, J.-Y. Courtois, and G. Grynberg, *Europhys. Lett.* **46**, 18 (1999).
- [20] R. Grimm, M. Weidemüller, and Y. Ovchinnikov, *Adv. At. Mol. Opt. Phys.* **42**, 95 (2000).
- [21] L. Guidoni and P. Verker, *J. Opt. B: Quantum Semiclass. Opt.* **1**, R23 (1999).
- [22] The imaginary part of the dynamic polarizability characterizes

the dissipative part of the atom-light interaction (i.e. spontaneous emission), and we assume that the detuning from atomic resonance is sufficiently large that this can be neglected on the duration of experiments (e.g. see [20]).

- [23] For a useful review of optical lattices and optical dipole forces we refer to reader to the review articles [20, 21].
- [24] E.g. see [4] and references therein.